What Causes Faster or Slower Offshore Propagation of Diurnal Rainfall in New Guinea?

ZIJIAN CHEN,[a] YU DU,[a,b,c] CLAIRE VINCENT,[d,e] EWAN SHORT,[d,e] HONGPEI YANG,[a] AND GUIXING CHEN[a]

[a] *School of Atmospheric Sciences, Sun Yat-sen University, and Southern Marine Science and Engineering Guangdong Laboratory (Zhuhai), Zhuhai, China*
[b] *Guangdong Province Key Laboratory for Climate Change and Natural Disaster Studies, Sun Yat-sen University, Zhuhai, China*
[c] *Key Laboratory of Tropical Atmosphere-Ocean System, Sun Yat-sen University, Ministry of Education, Zhuhai, China*
[d] *School of Geography, Earth and Atmospheric Sciences, University of Melbourne, Melbourne, Victoria, Australia*
[e] *ARC Centre of Excellence for 21st Century Weather, Melbourne, Victoria, Australia*

(Manuscript received 5 December 2025, in final form 27 March 2026, accepted 21 May 2026)

ABSTRACT: Twenty-year satellite observations have shown pronounced offshore propagation of the rainfall diurnal cycle at the northern coast of New Guinea. Propagation speed has a wide range from 5 to 15 m s^{-1} even when mean background winds are weak. This study investigates the mechanisms driving this variability in propagation speed, including why the slower-propagation rainfall events can travel more than 600 km, using the Maritime Continent Austral Summer Climatology v1.0, which provides 10-yr high-resolution model simulations. Days with pronounced propagation are analyzed, and the top 30% and bottom 30% of propagation speeds are classified as faster and slower cases, respectively. The faster-propagation group exhibits more widespread scattered rainfall patterns, primarily driven by inertia–gravity waves generated by land–sea thermal contrast. In this group, clearer skies allow greater daytime absorption of shortwave radiation, which amplifies the land–sea temperature contrasts and thereby generates stronger inertia–gravity waves that drive faster offshore rainfall propagation. Conversely, the slower group displays more concentrated rainfall, closely associated with cold pool dynamics farther offshore. Stronger low-level wind shear plays a key role in this group by favoring convection initiation along the leading edges of cold pools. The balance between low-level wind shear and cold pool intensity promotes more organized convection, whose offshore movement is primarily controlled by the cold pool propagation speed, resulting in slower but long-distance rainfall propagation. A key finding is that both inertia–gravity waves and cold pools can sustain offshore rainfall propagation over distances exceeding 600 km in New Guinea, in contrast to traditional studies that emphasize gravity waves as the primary driver of far-offshore propagation.

SIGNIFICANCE STATEMENT: Offshore-propagating rainfall is a defining feature in northern New Guinea, yet the physical mechanisms controlling its propagation speed remain poorly understood. Using long-term high-resolution model simulations, this study shows that rainfall systems can propagate more than 600 km offshore not only by inertia–gravity waves but also by cold pool dynamics under strong low-level wind shear. This finding challenges the conventional view that long-distance propagation is governed solely by gravity waves and provides new insight into the roles of cold pool dynamics and wave processes in organizing tropical convection. These insights deepen our understanding of diurnal rainfall propagation mechanisms and offer guidance for improving its representation in weather and climate models.

KEYWORDS: Inertia-gravity waves; Wind shear; Rainfall; Cold pools

1. Introduction

The diurnal cycle of convection is one of the most prominent features of tropical rainfall variability, particularly over the Maritime Continent (MC), where complex coastlines and topography strongly modulate local and regional weather systems (Dai 2001; Ohsawa et al. 2001; Yang and Slingo 2001; Neale and Slingo 2003; Nesbitt and Zipser 2003; Yang and Smith 2006; Kikuchi and Wang 2008; Johnson 2011; Ruppert et al. 2013; Short et al. 2019; Zhang and Du 2025). Offshore propagation of diurnal rainfall signals plays a crucial role in redistributing heat, moisture, and momentum between land and ocean, thereby influencing both short-term weather and longer-term climate processes (Houze et al. 1981; Johnson and Priegnitz 1981; Mapes and Houze 1993; Peatman et al. 2023). Although such offshore-propagating rainfall signatures have been observed along many coasts worldwide (Fang and Du 2022), the dominant mechanisms governing this phenomenon remain debated and have been attributed to several distinct physical processes.

Previous studies have identified a class of slowly propagating diurnal rainfall systems (i.e., 3–8 m s^{-1}) along tropical coastlines, typically attributed to density currents (Houze et al. 1981; Johnson and Bresch 1991; Sakurai et al. 2009; Fujita et al. 2011; Chen et al. 2016; Vincent and Lane 2016a; Coppin and Bellon 2019; Ruppert and Zhang 2019). These density currents generally originate from evaporative cooling beneath deep convection (e.g., cold pool outflows) or radiative cooling of the nocturnal surface layer (e.g., land breeze). As these dense air masses spread seaward, they lift moist marine air along their

Corresponding author: Yu Du, duyu7@mail.sysu.edu.cn

DOI: 10.1175/JAS-D-25-0232.1

leading edges, initiating new convection and sustaining offshore propagation. The interaction of evaporative cold pools with sea breezes can further enhance offshore movement by providing additional low-level convergence. The efficiency of these processes, however, depends strongly on environmental conditions, such as vertical wind shear and ambient stability, which modulate both the propagation distance and convection intensity. Typically, density-current-driven systems are generally thought to be confined to short offshore distances (i.e., 100–200 km from the coast; Vincent and Lane 2016a).

In contrast, faster-propagating rainfall systems (i.e., 10–20 m s^{-1}) have been linked to the influence of inertia–gravity waves triggered by land–sea thermal contrasts and land-based convection (Tripoli and Cotton 1989; Mapes et al. 2003; Ichikawa and Yasunari 2007; Love et al. 2011; Du and Rotunno 2015; Li and Carbone 2015; Hassim et al. 2016; Vincent and Lane 2016a; Birch et al. 2016; Vincent and Lane 2018; Ruppert and Zhang 2019; Ruppert et al. 2020; Peatman et al. 2023; Peng and Chen 2023, 2024, 2025). These waves can organize and propagate convective disturbances hundreds of kilometers offshore, sometimes exceeding 600 km from the coastline (Chen and Du 2024). Unlike density currents, which rely on mechanical lifting of moist air, gravity waves generate oscillatory motions that can precondition the offshore environment for deep convection. Their upward phase enhances local instability and vertical motion, thereby triggering new convection. The generation and propagation of such waves are also modulated by background winds, boundary layer stability, and topography (Qian et al. 2009, 2012; Jiang 2012; Du and Rotunno 2015, 2018; Du et al. 2019; Du 2023; Chen and Du 2024; Du et al. 2024; Chen et al. 2025), leading to distinct differences in propagation speed, structure, and rainfall intensity. Understanding the relative contributions of these mechanisms is therefore essential to explain the diversity of offshore rainfall behavior.

Previous studies across the MC have revealed that diurnal rainfall propagation speeds can vary over a wide range. For instance, Peatman et al. (2023) showed that along the southwestern coast of Sumatra, composite propagation signals exhibit speeds from ~2 m s^{-1} at the slow end to more than 13 m s^{-1} at the fast end. This variability cannot be explained solely by averaging effects or directional differences, and it may indicate the diversity in propagation mechanisms. Multiple propagation modes, such as density current and gravity waves, may coexist or dominate at different distances from the coast (Vincent and Lane 2016a, 2017; Yokoi et al. 2017; Coppin and Bellon 2019). Even within a single mode, the propagation speed can fluctuate with environmental factors, including wind shear, thermal contrast, and moisture distribution (Jiang 2012; Du et al. 2019; Chen et al. 2025). Consequently, offshore propagation of rainfall diurnal signals is better characterized as a continuum of speeds governed by different processes rather than a single representative velocity. Understanding what determines faster and slower propagations is therefore essential to unraveling the dynamics of the diurnal rainfall cycle in coastal areas.

In addition to variations in propagation speed, offshore extent also differs depending on the dominant mechanisms. Bai et al. (2021) showed that along the southwestern coast of Sumatra, rainfall systems can propagate up to 180 km offshore at speeds of 4.5 m s^{-1}, primarily driven by the interaction of land breeze and background winds. Peatman et al. (2023) suggested that the combined effects of land breeze and cold pools can sustain propagation of ~3 m s^{-1} for 200–300 km. Similarly, Hassim et al. (2016) found that rainfall over northern New Guinea can extend up to 200 km offshore at speeds of 3–6 m s^{-1} in both observations and model simulations, associated with land-breeze convergence. Vincent and Lane (2016a) also showed that precipitation within 100–200 km from the northern coast of New Guinea propagates offshore as a squall line driven by katabatic flow and the land breeze (3–5 m s^{-1}), while farther offshore (400–700 km), faster systems (12–18 m s^{-1}) are associated with inertia–gravity waves. In the Bay of Bengal, Chen and Du (2024) reported rainfall propagation exceeding 900 km under the influence of gravity waves. Collectively, these findings suggest that density-current-driven systems generally propagate shorter distances than those influenced by gravity waves.

In this study, we found that rainfall over New Guinea can propagate more than 600 km at speeds of around 8 m s^{-1}, while comparable distances are also reached by faster speeds. Previous studies have not clearly identified the mechanisms responsible for such long-distance propagation at relatively slow speeds. Therefore, understanding the physical nature and governing factors of these propagating rainfall systems can provide valuable insight into the mechanisms controlling diurnal offshore rainfall propagation.

Here, we examine the mechanisms controlling rainfall propagation speed through satellite rainfall observations and a cloud-permitting numerical model. Prominent rainfall propagation events are selected, and their propagation speeds are estimated by tracking the diurnal peak of rainfall in Hovmöller diagrams, following the methods of previous studies (Fang and Du 2022; Peatman et al. 2023). We then assess how cold pool processes and gravity wave dynamics contribute to the observed variability in propagation speed.

The remainder of this paper is organized as follows. Section 2 describes the dataset and analysis method. Section 3 presents the characteristics of rainfall events with different propagation speeds. Section 4 discusses the mechanisms controlling propagation speed. Finally, section 5 provides a summary and discussion of our findings.

2. Data and methodology

a. Data

This study employs a 10-yr austral summer cloud-permitting simulation over the Maritime Continent region (hereafter MCASClimate). This dataset, described by Vincent and Lane (2016b, 2017), was generated using the Weather Research and Forecasting (WRF) Model, version 3.5 (Skamarock and Klemp 2008). The simulation consists of continuous 3-month integrations for 10 austral summer seasons (December–February of 2005/06–2014/15).

The simulations are forced by European Centre for Medium-Range Weather Forecasts (ECMWF) interim reanalysis (ERA-Interim; Dee et al. 2011) as initial and lateral boundary conditions, with an outer domain of 12-km horizontal grid spacing, a

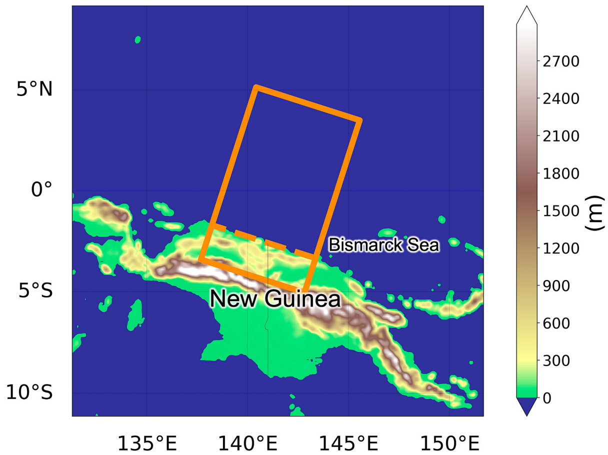

FIG. 1. The study domain (orange box) and terrain elevation (shading). The dashed orange line represents the coastline along northern New Guinea.

nested domain of 4-km horizontal grid spacing, and 79 vertical levels with a model top at 25 km. Spectral nudging was applied in the 12-km domain to maintain large-scale consistency with ERA-Interim, where only horizontal scales longer than 1000 km above the boundary layer were nudged, using an inverse nudging time scale of 0.0003 s^{-1} for all variables. The physical parameterizations include the WSM6 microphysics scheme (Hong and Lim 2006), the MYJ planetary boundary layer scheme (Mellor and Yamada 1982), the RRTM longwave (Mlawer et al. 1997), and Goddard shortwave radiation (Chou and Suarez 1994) schemes. The Betts–Miller–Janjić cumulus scheme (Janjić 1994) was used in the outer domain only. Further details of the model setup are described in Vincent and Lane (2017).

The analysis in this study focuses on the northern coast of New Guinea and the adjacent oceanic region (indicated by the orange box in Fig. 1). To investigate the mechanisms controlling rainfall propagation, we analyze the 10-yr MCASClimate output fields, including the three-dimensional wind components (U, V, and W), pressure, potential temperature, geopotential height, hourly rainfall rate, outgoing longwave radiation (OLR), and surface upward turbulent sensible heat flux (HFX).

Additionally, we employ the Global Precipitation Measurement Integrated Multi-satellitE Retrievals (GPM-IMERG) precipitation product (Huffman et al. 2015), with a spatial resolution of 0.1° × 0.1° and a temporal resolution of 30 min. This dataset is utilized for both validation and comparison of the diurnal rainfall propagation characteristics. All times are reported in local standard time (LST), corresponding to Papua New Guinea's time zone of UTC + 10.

b. *Wave filtering algorithm*

In this study, we employ a dispersion-consistent filtering algorithm to isolate inertia–gravity wave signals from background noise. This approach builds upon the methods of Kruse and Smith (2015), Lane (2021), Yang and Du (2024), and Peng and Chen (2025). We first define a right-hand (x, y, z) coordinate system, where x is the coastline perpendicular direction, with increasing x moving offshore, y is the coastline parallel direction, and z is the vertical direction. The data are first averaged along the y direction, and a filter is subsequently applied to the averaged field. Our filtering algorithm then consists of three primary steps:

1) For a given function a, we perform a 2D Fourier decomposition from (x, z) space to (k–m) space, yielding its spectral power $\hat{a}(k, m)$, where k and m are the horizontal and vertical wavenumbers, respectively.
2) These 2D spectral power $\hat{a}(k, m)$ are then multiplied by a Gaussian low-pass response function $\hat{r}_{\mathrm{lp}}(k, m)$:

$$\hat{a}_{\mathrm{lp}}(k, m) = \hat{a}(k, m) \times \hat{r}_{\mathrm{lp}}(k, m). \quad (1)$$

The Gaussian low-pass response function is defined as

$$\hat{r}_{\mathrm{lp}}(k, m) = \hat{r}_{\mathrm{lp}x}(k) \times \hat{r}_{\mathrm{lp}z}(m), \quad (2)$$

where $\hat{r}_{\mathrm{lp}x}(k)$ is the horizontal filtering operator and $\hat{r}_{\mathrm{lp}z}(m)$ is the vertical filtering operator. The horizontal filtering operator is defined in wavenumber space as

$$\hat{r}_{\mathrm{lp}x}(k) = e^{-|k|^2 L^2}, \quad (3)$$

where L is the cutoff wavelength.
3) To incorporate the vertical scale consistent with gravity wave dynamics, we map the vertical wavenumber m to an equivalent horizontal wavenumber $k_z(m)$ using the inertia–gravity wave dispersion relation [Eq. (35) in Chen et al. 2025]:

$$k_z(m) = m\sqrt{\frac{\sigma^2 - f^2}{N^2 - \sigma^2 + f^2}}, \quad (4)$$

where N is the Brunt–Väisälä frequency and f is the Coriolis parameter. The intrinsic frequency σ is defined as

$$\sigma = \omega - KU, \quad (5)$$

where $\omega = 2\pi/T$, $T = 24$ h is the period of diurnal heating, $K = \sqrt{k^2 + m^2}$ is the wavenumber, and U is the background wind. The corresponding vertical filtering operator is then defined as

$$\hat{r}_{\mathrm{lp}z}(m) = e^{-|k_z(m)|^2 L^2}. \quad (6)$$

Finally, an inverse Fourier transform is applied to obtain the filtered field in physical space.

This dispersion-consistent approach prevents overfiltering of gravity waves in the vertical direction, a common issue when directly applying a 2D filter based on $k^2 + m^2$ (Kruse and Smith 2015). Because gravity waves relevant to rainfall propagation typically have horizontal wavelengths of 600–1200 km but much shorter vertical wavelengths of 4–7 km (Chen et al. 2025), conventional filters would suppress nearly all vertical modes. By mapping vertical wavenumbers through the dispersion relation, our method preserves both horizontal and vertical gravity wave

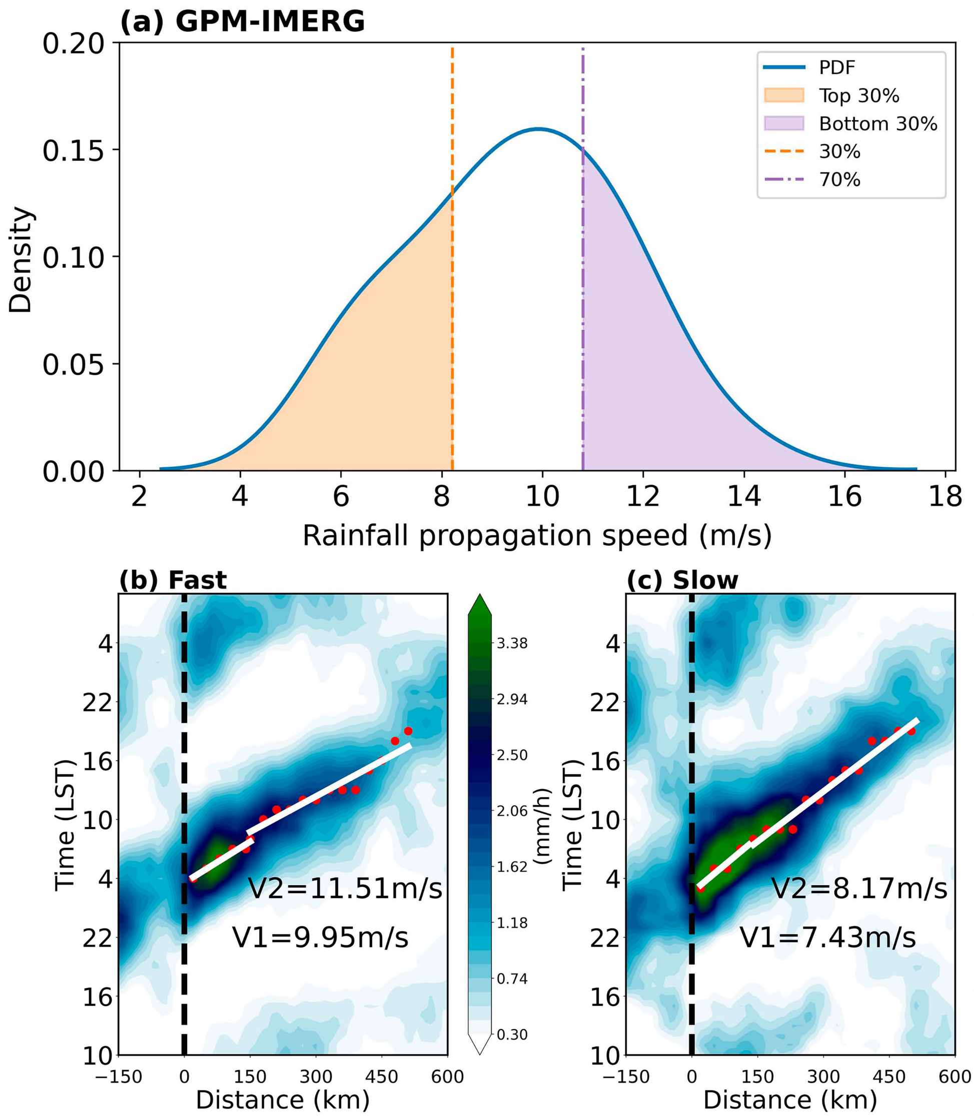

FIG. 2. (a) Probability density distribution of offshore rainfall propagation speeds derived from GPM-IMERG satellite rainfall data. Hovmöller diagrams of composite rainfall (shading; mm h^{-1}) for (b) fast and (c) slow offshore-propagating rainfall events. The red dots indicate the diurnal hour of maximum rainfall, and the white line is the regression line fitted to the red dots, with its slope representing the rainfall propagation speed. The black dashed line represents the location of the coastline. V1 represents the average rainfall propagation speed within 150 km of the coastline, and V2 represents the average speed beyond 150 km.

structures while removing small-scale noise, ensuring that the retained signals remain dynamically consistent with gravity wave physics.

3. Comparisons of fast and slow diurnal offshore rainfall propagation

a. Observations

Diurnal offshore rainfall propagation events are a prominent feature around New Guinea (Fang and Du 2022). We derive the probability density function (PDF) of rainfall propagation speeds using GPM-IMERG precipitation data from December to February during 2002–23. Figure 2a shows that the derived PDF of propagation speeds exhibits a broad distribution of propagation speeds, typically ranging between 5 and 15 m s^{-1} under weak offshore background wind conditions (i.e., 0–2 m s^{-1}, perpendicular to the coastline). The background wind is calculated as the mean wind averaged between 850 and 300 hPa, following the approach of Fang and Du (2022). This widespread of propagation speeds indicates that background winds alone cannot fully explain the observed variability, and other factors may modulate rainfall propagation over this region.

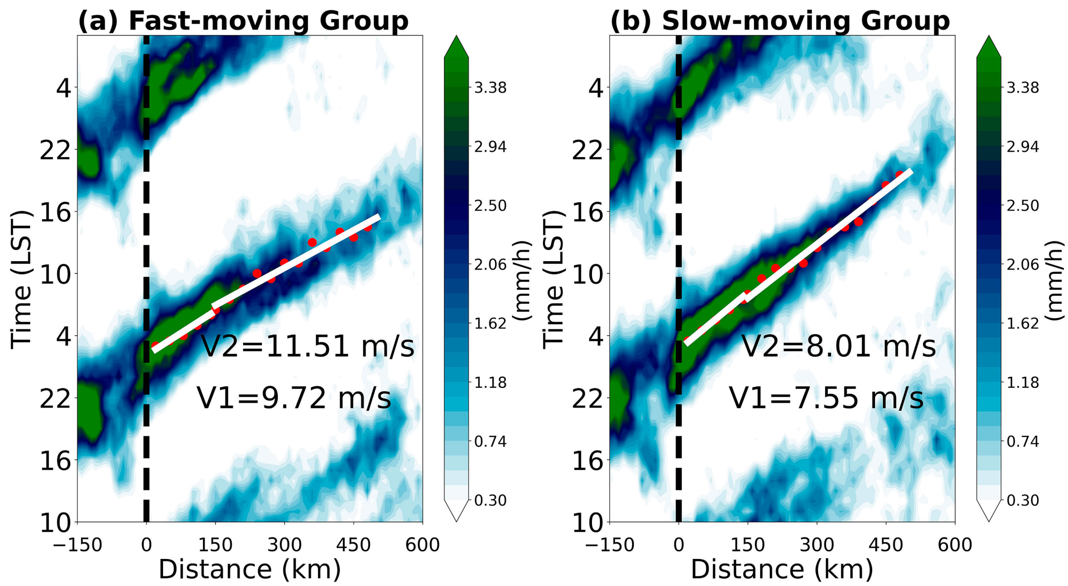

FIG. 3. Hovmöller diagrams of composite rainfall (shading; mm h^{-1}) for (a) the fast-moving group and (b) the slow-moving group, calculating from the MCASClimate dataset following the same method as in Fig. 2.

Based on the PDF, rainfall propagation events are categorized into fast and slow groups, corresponding to the fastest 30% and slowest 30% of all events under weak background wind conditions (indicated by the yellow and purple shading in Fig. 2a). Composite Hovmöller diagrams for these two groups reveal distinct propagation characteristics (Figs. 2b,c). In both composites, rainfall typically initiates over land around 1900 LST and begins to propagate offshore at approximately 2200 LST near the coastline. For the fast group, the average propagation speed is about 9.95 m s^{-1} nearshore (within 150 km of the coastline; V1 in Fig. 2b) and increases slightly to 11.51 m s^{-1} farther offshore (beyond 150 km; V2 in Fig. 2b). In contrast, the slow group exhibits average speeds of 7.43 m s^{-1} nearshore and 8.17 m s^{-1} farther offshore (V1 and V2 in Fig. 2c).

Nearshore rainfall propagation is commonly attributed to density currents, such as cold pools (e.g., Houze et al. 1981; Fujita et al. 2011; Hassim et al. 2016; Vincent and Lane 2016a; Ruppert and Zhang 2019; Fang and Du 2022), which are typically associated with slower propagation speeds and short propagation distances. Farther offshore propagation, by contrast, is often explained by diurnal gravity waves, characterized by faster speeds and longer propagation distances. However, in the slow group, rainfall located beyond 150 km offshore (Fig. 2c) propagates at only about 8 m s^{-1}, comparable to typical cold pool speeds. This discrepancy suggests that density currents may play a role in influencing or sustaining rainfall propagation even at relatively large offshore distances, indicating that the mechanisms controlling offshore propagation are more complex than a simple nearshore–offshore distinction.

b. *Regional climate model results*

To further investigate the factors influencing rainfall propagation, we analyze simulations from the MCASClimate dataset. Propagation events are classified according to their speeds using the same method as in Fig. 2. The fastest 30% of events are defined as the fast-moving group, while the slowest 30% as the slow-moving group, with both groups selected under weak background wind conditions.

The composite Hovmöller diagrams of simulated rainfall from these two groups (Fig. 3) exhibit different propagation characteristics and show good agreement with the observed rainfall in Fig. 2. In the fast-moving group, rainfall derived from both GPM-IMERG (Fig. 2b) and MCASClimate (Fig. 3a) propagates at approximately 10 m s^{-1} nearshore and increases slightly to about 11.5 m s^{-1} beyond 150 km offshore. In the slow-moving group, propagation speeds are around 7.5 m s^{-1} nearshore and 8 m s^{-1} farther offshore.

In both groups, rainfall begins propagating in the early evening and extends more than 600 km from the coastline. Even in the slow-moving group, rainfall maintains a long propagation distance despite its slower speed (~8 m s^{-1}). Notably, rainfall intensity in the far-offshore region (150–600 km) is stronger in the slow-moving group than in the fast-moving group, suggesting that the former is supported by organized deep convection, whereas the latter is primarily associated with weaker convection. This feature is also evident in the observed rainfall shown in Fig. 2c.

The spatial distribution of rainfall over New Guinea for the simulated fast-moving and slow-moving groups is shown in Fig. 4. In both groups, most rainfall occurs over the coastline around midnight (Figs. 4a,e). Convection triggered by density currents subsequently propagates offshore in the form of a squall line during the early morning (Figs. 4b,f), resulting in substantial rainfall in the nearshore region. These near-coastal precipitation characteristics are consistent with those reported by Hassim et al. (2016), who investigated the processes leading to offshore rainfall in New Guinea.

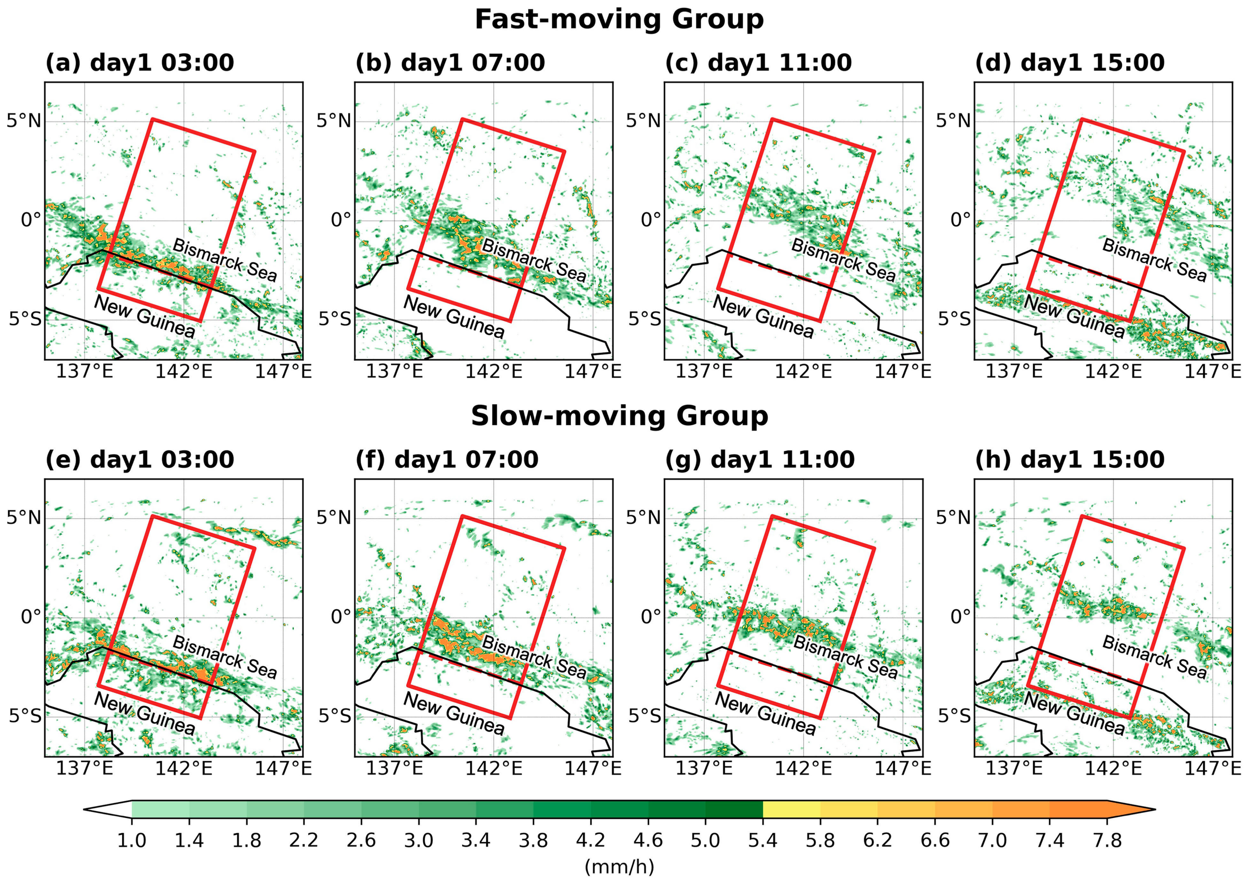

FIG. 4. Composite rainfall distribution (shading; mm h^{-1}) derived from the MCASClimate dataset. The red box represents the analysis area, and the dashed line indicates the coastline.

In the slow-moving group, the coherent squall line continues to propagate offshore for more than 500 km until the afternoon, with substantial rainfall accumulations extending into the Bismarck Sea near 0° latitude (Fig. 4h). The structure and propagation speed of rainfall remain consistent from the coast to the open ocean, and rainfall stays well organized and concentrated. This suggests that a common mechanism, likely density current dynamics, governs rainfall propagation across both nearshore and offshore regions.

In contrast, rainfall in the fast-moving group becomes increasingly scattered beyond 150 km offshore (Fig. 4d). Rainfall intensity decreases relative to near-coast values, while the propagation speed remains higher, suggesting that gravity waves play a key role in driving the offshore rainfall in this group. The evolution of rainfall in the fast-moving group is consistent with previous studies (e.g., Fang and Du 2022), which found that nearshore rainfall is primarily supported by density currents and subsequently guided offshore by gravity waves.

To investigate the environmental factors influencing rainfall propagation speed in the two groups, cross sections of wind anomalies are presented in Fig. 5. The blue clockwise-turning arrows in Figs. 5a and 5f indicate sea-breeze circulations near the coastline at 1200 LST, which subsequently extend offshore up to 600 km by 1800 LST. A similar phenomenon is observed at night, as indicated by the red counterclockwise-turning arrows in Figs. 5c, 5d, 5h, and 5i. Land-breeze circulations develop around 0000 LST in the coastal area and then extend offshore. Consistent features are also evident in ERA5 reanalysis (not shown), supporting the robustness of this behavior. This diurnal expansion of the wind circulation is consistent with inertia–gravity wave behavior, as discussed by Rotunno (1983), who demonstrated that land–sea breeze circulations at latitudes below 30° can act as oscillatory gravity waves that propagate away from the coast.

Offshore winds below 2 km are relatively strong near the coast at 0000 and 0600 LST. The pronounced horizontal wind gradient at these hours likely results from the combined effects of density currents and land-breeze circulations. The leading edge of the strong wind region generates pronounced low-level convergence, which favors convection initiation.

In the fast-moving group (Fig. 5e), the land-breeze circulation propagates offshore more rapidly than in the slow-moving group (Fig. 5j), but its offshore wind intensity is weaker. This distinction in low-level wind structure between the two groups likely contributes to their contrasting rainfall propagation speeds. To further assess this relationship, the background wind and low-level wind shear characteristics are examined in the following section.

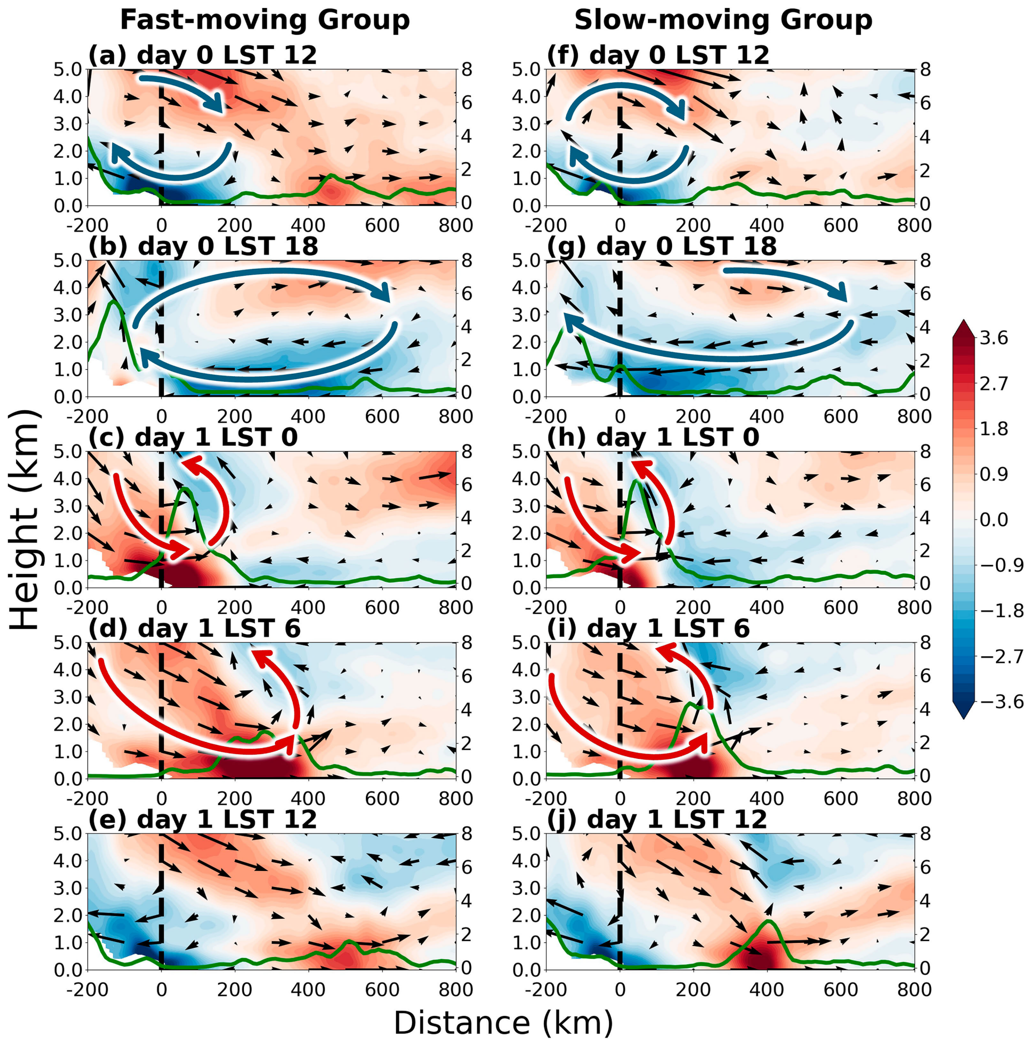

FIG. 5. Diurnal composite vertical cross sections perpendicular to the coast of horizontal wind anomaly (shading; m s^{-1}) and vertical wind anomaly (vectors) averaged over the orange box in Fig. 1 derived from the MCASClimate dataset. The green solid line indicates rainfall. The blue and red turning arrows indicate the sea-breeze and land-breeze circulations, respectively. The black dashed line indicates the location of the coastline.

The vertical profiles of background wind averaged over the ocean (0–800 km offshore) are shown in Fig. 6a. Both groups exhibit pronounced wind shear below 3 km. In the fast-moving group, winds are near calm at the surface and gradually become offshore with altitude, reaching a maximum offshore wind of approximately 3 m s^{-1} around 2 km. In contrast, the slow-moving group features onshore winds of about 2 m s^{-1} near the surface, which transition to offshore flow aloft, peaking around 3.5 m s^{-1} at 3 km. The presence of stronger onshore winds near the surface in the slow-moving group results in enhanced low-level wind shear. This shear environment is likely modulated by the low-level northwesterly cross-equatorial winds and the midlevel southwesterly winds associated with the South Pacific convergence zone (SPCZ) and the Australian monsoon trough during the passage of the Madden–Julian oscillation (MJO), with additional contributions from the land–sea breeze perturbation (Ichikawa and Yasunari 2008; Dao et al. 2026).

This difference is further confirmed by the boxplot of 0–3-km wind shear (Fig. 6b), calculated from the averaged winds ahead of convection (0–200 km offshore), at the time when the convective system propagates over the ocean. The median shear in the slow-moving group is 5.4 m s^{-1}, nearly double that of the fast-moving group (2.9 m s^{-1}). In addition, the narrower interquartile range in the slow-moving group suggests more uniform and consistently stronger shear conditions.

At the furthest offshore edge of the density current, the vorticity associated with the advancing current flow opposes the vorticity generated by the 0–3-km ambient shear. Suppose, for argument's sake, the current-generated vorticity is at least comparable in magnitude to the ambient shear for the slow-moving group (~5 m s^{-1}). Under such conditions, and

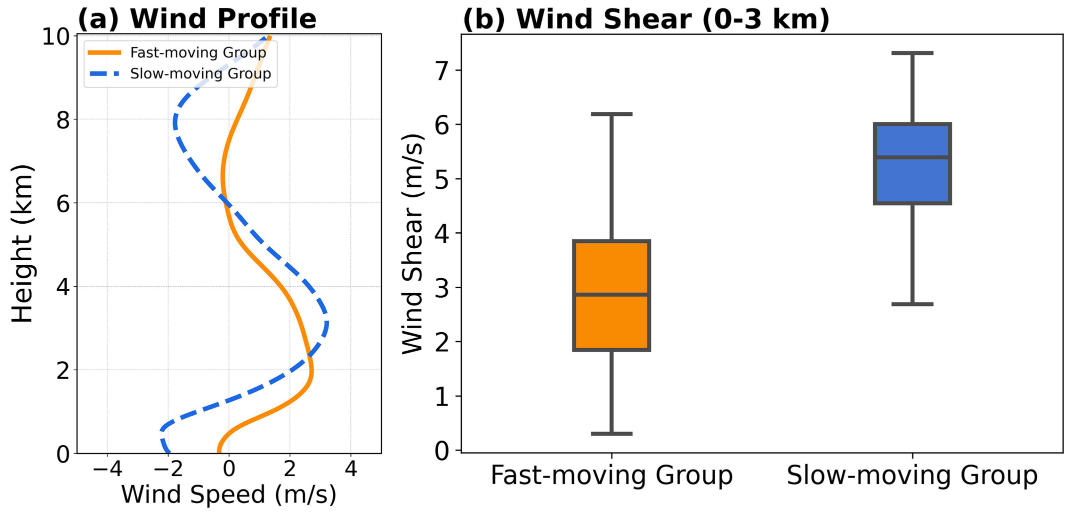

FIG. 6. (a) Vertical profiles of mean background wind (m s^{-1}) and (b) boxplots of 0–3-km wind shear for the fast- and slow-moving groups.

as depicted in Fig. 6, we would expect stronger lifting of low-level parcels at the leading edge of the cold pool in the high-shear group (slow-moving group) than the low-shear group (fast-moving group), in accordance with Rotunno–Klemp–Weisman (RKW) theory (Rotunno et al. 1988; Weisman and Rotunno 2004; Bryan et al. 2006; Bryan and Rotunno 2014). We therefore hypothesize that in the high-shear cases, convection is more effectively organized into squall-line-type systems than in the low-shear cases. These squall lines produce most of rainfall in the high-shear cases and contribute to the slower offshore propagation speeds relative to the low-shear cases.

It is worth noting that the propagation speed difference in Fig. 3 is similar to the difference in the boundary layer wind (below 1 km; Fig. 6a), which may contribute to the difference in propagation speed. To examine this further, we subtracted the average boundary layer wind from the propagation speed of each individual event, and the results show that the average propagation speed difference between the fast-moving and slow-moving groups is reduced. Specifically, the two groups differ by approximately 4 m s^{-1} before the removal, whereas the difference decreases to approximately 2.4 m s^{-1} after the removal. This indicates that the boundary layer wind does contribute to the difference in propagation speed between the two groups, but it is not the sole factor controlling the propagation speed.

In the following section, we further examine the dynamics of cold pools in long-distance rainfall propagation to clarify the mechanisms responsible for differences in propagation speed.

4. Mechanisms driving different propagation speeds

In this section, we investigate the mechanisms that drive rainfall propagation and its associated speed. We first examine the role of cold pools in both nearshore and far-offshore rainfall propagation. Next, we assess the influence of gravity waves on rainfall propagation in the fast- and slow-moving groups. Finally, we explore how low-level winds associated with cold pools modulate the rainfall propagation speed in the two groups. Together, these analyses aim to clarify the processes controlling rainfall propagation in this region.

a. *Influence of cold pools*

Cold pools play a key role in initiating convection during nearshore rainfall propagation. Previous studies (e.g., Hassim et al. 2016; Peatman et al. 2023) have shown that new convection preferentially develops along the leading edge of density currents, such as cold pools. In coastal regions, cold pools typically form as heavy afternoon rainfall produces strong evaporative cooling over land and radiative cooling after sunset, generating dense air that subsequently spreads seaward. The expansion of these cold pools promotes the development and organization of convection, thereby driving the nearshore propagation of squall lines, as illustrated in Fig. 4. Beyond their nearshore effects, we further investigate how cold pools contribute to rainfall propagation in far-offshore regions, where they form primarily through evaporative cooling from oceanic convective rainfall.

The vertical structures of cold pools in the fast- and slow-moving groups are illustrated in Fig. 7, using composite cross sections of buoyancy anomaly. Cold pools are identified based on thermal buoyancy B, defined following Du et al. (2020): $B = g[(\theta_v - \overline{\theta_v})/\overline{\theta_v}]$, where θ_v is the virtual potential temperature, $\overline{\theta_v}$ is its horizontal mean over the orange box in Fig. 1 representing the environmental virtual potential temperature (Du et al. 2020), and g is the gravitational acceleration. The theoretical cold pool intensity (or theoretical propagation speed) C is estimated following Grant and van den Heever (2016): $C^2 = 2\int_0^H(-B)dz$, where H represents the cold pool depth, defined as the height at which $|B| \leq 0.01$ m s^{-2}, corresponding to the top of the cold pool shown in Fig. 7. The low-level wind shear (U_s) in Fig. 7 is calculated as the wind difference between 0 and 3 km, horizontally averaged over the 200-km

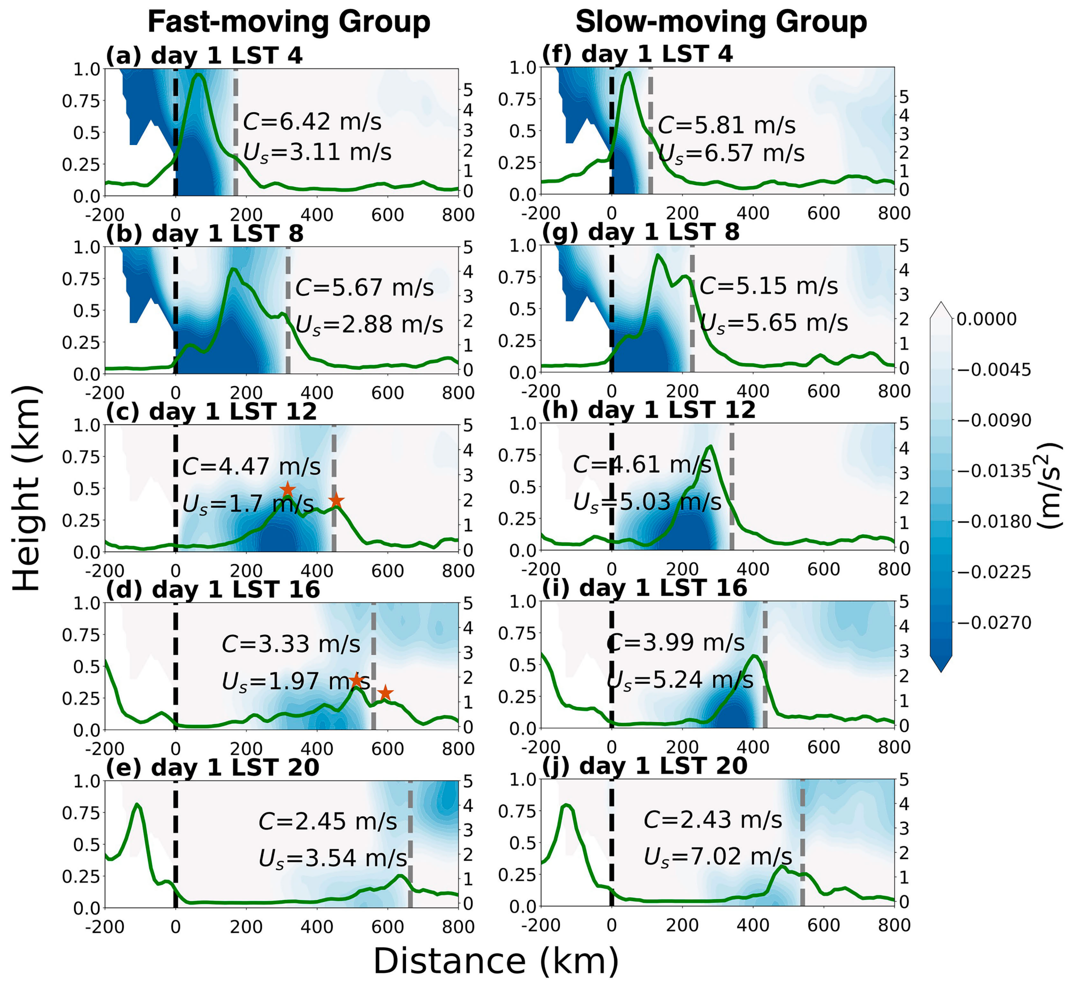

FIG. 7. Diurnal composite vertical cross sections perpendicular to the coast of buoyancy anomaly (shading; m s^{-2}) averaged over the orange box in Fig. 1 derived from the MCASClimate dataset. The green solid line indicates rainfall. The gray dashed lines mark the leading edge of the cold pool, defined as the location where near-surface buoyancy equals zero. The brown stars represent the peaks of rainfall. The black dashed line indicates the coastline. C indicates the theoretical intensity of the cold pool, and U_s represents the mean 0–3-km wind shear averaged over the region 0–200 km ahead of the cold pool leading edge.

region ahead of the cold pool's leading edge at the corresponding time.

Figures 7a and 7f illustrate the cold pool structures when the precipitation systems are located near the coast. The cold pools in the fast-moving group are initially stronger, likely due to more intense daytime convection over land, which generates heavier rainfall and stronger evaporative cooling. However, between 1200 and 1600 LST, the slow-moving group exhibits slightly stronger cold pools. By 2000 LST, when the precipitation systems have propagated more than 500 km offshore, the cold pool intensities in both groups become comparable.

These results suggest that beyond approximately 300 km from the coast, the slow-moving group sustains stronger precipitation (green contours in Fig. 7) and more pronounced cold pools. Moreover, the vertical wind shear (U_s) in the slow-moving group remains consistently stronger than in the fast-moving group. It is worth noting that the ratio of cold pool intensity C and low-level wind shear U_s shown in Fig. 7 is close to 1 ($C/U_s \approx 1$) in the slow-moving group (Figs. 7f–i). Even when considering wind shear calculated between 0 and 2, 0 and 4, and 0 and 5 km, values range plausibly from 2.8 to 6.0 m s^{-1} in the slow-moving group and from 0.4 to 4.0 m s^{-1} in the fast-moving group. According to RKW theory (Rotunno et al. 1988; Weisman and Rotunno 2004; Bryan et al. 2006; Yang and Du 2026), the deepest lifting along the cold pool leading edge and the most effective convective retriggering occur when C and U_s are nearly balanced. This "optimal" balance promotes strong, organized, and long-lived squall lines, thereby supporting the sustained yet slower rainfall propagation observed in the slow-moving group. By contrast, in the fast-moving group, wind shear is generally too weak relative to cold pool intensity. These contrasts in cold pool intensity and vertical wind shear between the two groups are also evident in ERA5 reanalysis (not shown), further supporting the robustness of the simulated results.

In the slow-moving group, a single rainfall peak (green line in Fig. 7) appears near or just behind the cold pool's leading edge (gray dashed line in Fig. 7), even when rainfall propagates far offshore (Figs. 7g–j). In contrast, the fast-moving group exhibits two distinct rainfall peaks at 1200 and 1600 LST (brown stars in Figs. 7c,d). The rear peak, located just behind the cold pool's leading edge, is associated with cold-pool-induced convection, whereas the weaker forward peak ahead of the leading edge is probably linked to gravity wave forcing. This rainfall behavior in the fast-moving group is consistent with previous findings (e.g., Fang and Du 2022).

Since frontal dynamics alone cannot easily distinguish between a cold pool edge and a land-breeze front, we examine the downdraft intensity behind the leading edge (Fig. 7) to assess whether cold pools are more active in the slow-moving group. Figure 8 shows boxplots of the mean downdraft intensity (vertically averaged from the surface to 2 km within 200 km behind the leading edge) for both groups. The median downdraft intensity in the slow-moving group is approximately 40% stronger than that in the fast-moving group, suggesting that cold pools are more active in the slow-moving group, consistent with a stronger density current character that is more effective in sustaining and organizing rainfall propagation.

Unlike previous studies (e.g., Peatman et al. 2023), which suggested that density currents primarily contribute to nearshore rainfall within ~200 km of the coastline, we find that under strong low-level wind shear, cold pools can initiate and sustain convection propagating much farther offshore, extending beyond 600 km from the coast. However, given that gravity waves are widely recognized as a key mechanism driving long-distance offshore propagation, in the next section, we examine the role of gravity waves in modulating rainfall propagation in both groups.

b. *Influence of gravity waves*

To understand how gravity waves influence offshore rainfall propagation and why they are less dominant in the slow-moving group, we examine the differences in the surface radiative effects between the two groups. Figure 9 presents the daytime distribution of OLR. Compared with the slow-moving group, the fast-moving group exhibits substantially higher OLR values over land during the daytime (Figs. 9a,b). At 1400 LST, most land areas reach an OLR of about 274 W m^{-2}, indicating stronger solar heating at the surface. By 2200 LST, OLR values over land decrease markedly in the fast-moving group, dropping to around 100 W m^{-2} across much of the region. This pronounced reduction implies the presence of higher cloud tops and deeper convection in the evening. Such strong land-based convection generates more intense cold pools and promotes a rapid decrease in land surface temperature, which in turn enhances the land–sea thermal contrast in the fast-moving group.

The diurnal variation of OLR and HFX averaged over land (purple box below the dashed line in Fig. 9) is shown in Fig. 10. In both groups, OLR peaks around 1300 LST on day 0 and reaches a minimum near 2300 LST. The fast-moving group (orange line in Fig. 10a) exhibits a peak OLR approximately 20 W m^{-2} higher than the slow-moving group, while its

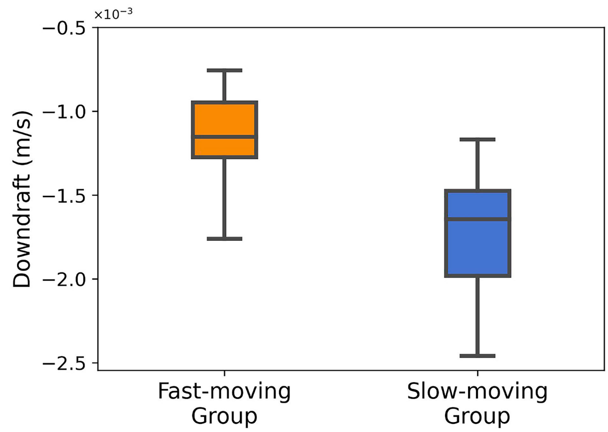

FIG. 8. Boxplots of the average downdraft (m s^{-1}) within 200 km behind the leading edge of the cold pool, from the surface to 2 km, for the fast- and slow-moving groups.

nighttime minimum is about 17 W m^{-2} lower, consistent with the spatial patterns in Fig. 9. This OLR difference indicates reduced daytime cloud cover over land in the fast-moving group, allowing greater shortwave solar radiation to heat the land surface. As shown in Fig. 10b, the fast-moving group exhibits stronger HFX at noon, consistent with the enhanced daytime OLR. The difference in HFX between the two groups (purple line in Fig. 10b) shows that daytime HFX in the fast-moving group is about 23 W m^{-2} higher than in the slow-moving group. This enhanced daytime surface heating strengthens the land–sea thermal contrast in the fast-moving group, which can contribute to the generation of stronger gravity waves than in the slow-moving group.

Given the higher daytime OLR and HFX over land in the fast-moving group, we next examine the land–sea thermal contrast, which is a key factor modulating the characteristics of gravity waves. The diurnal variation of the land–sea surface temperature difference between the ocean and land in the two groups, as well as their difference, is shown in Fig. 11. The intergroup difference (purple line in Fig. 11) indicates that temperature difference in the fast-moving group is nearly 1.5 K larger than in the slow-moving group at 1000 LST, reflecting stronger daytime solar heating and HFX over land. By 2300 LST, temperature difference in the fast-moving group decreases, likely due to evaporative cooling associated with evening rainfall over land. These results suggest that gravity waves induced by the enhanced land–sea thermal contrast in the fast-moving group are stronger and may contribute more significantly to offshore rainfall propagation.

The diurnal variation of gravity wave patterns is shown in Fig. 12 using vertical cross sections of low-pass-filtered potential temperature anomalies. The cutoff wavelength of the low-pass filter, introduced in section 2, is set to 650 km, consistent with the gravity wave wavelengths described in Chen et al. (2025). Gravity waves are visualized through the vertical structure of potential temperature anomalies (Fig. 12), with signals resembling gravity wave modes extending along ray paths from the coastline over the ocean (gray lines in Fig. 12),

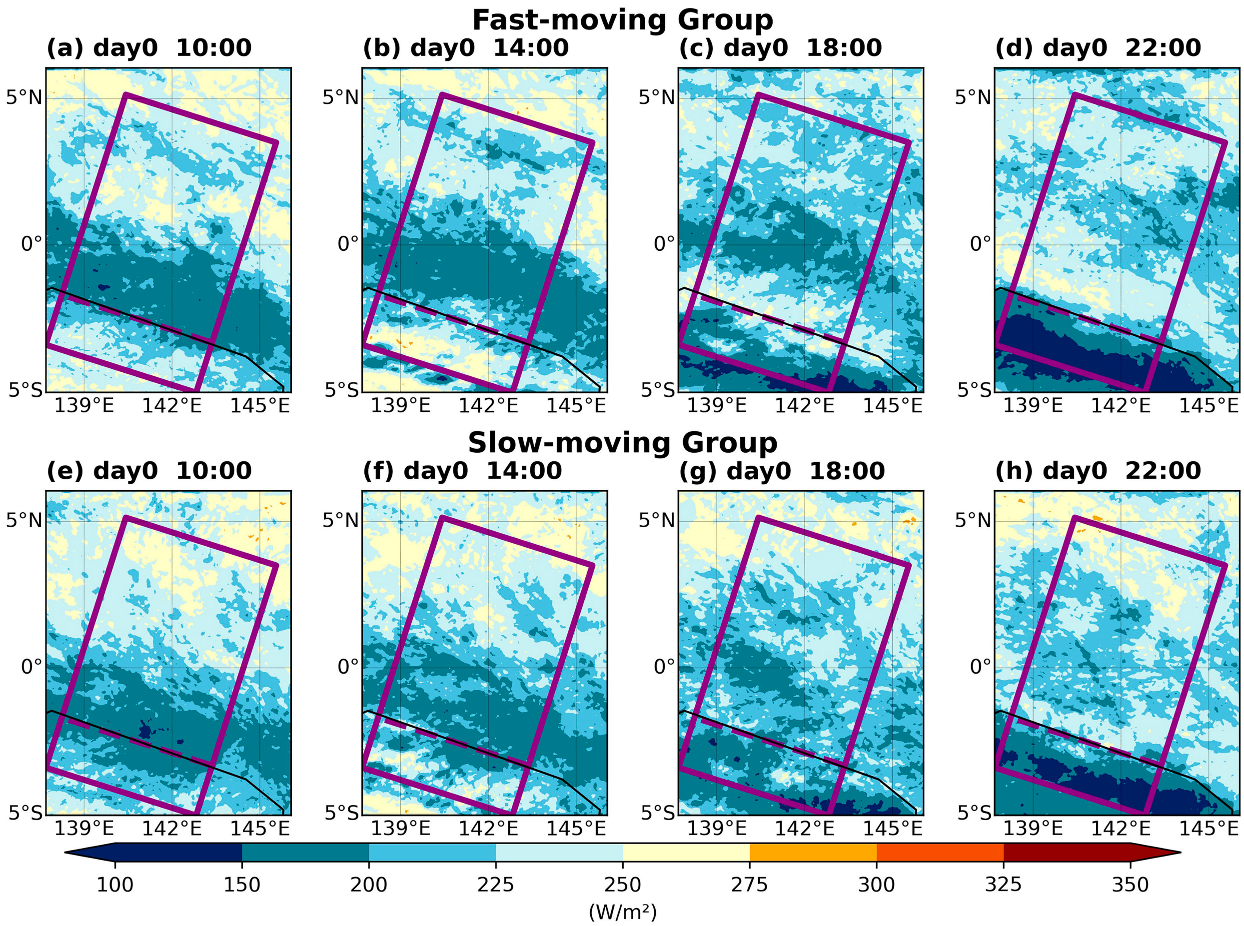

FIG. 9. Composite distribution of OLR (shading; W m^{-2}) derived from the MCASClimate dataset. The purple solid box represents the study area, and the purple dashed line indicates the coastline.

similar to those reported by Rotunno (1983) and Chen et al. (2025).

In both groups, at 1500 LST, diagonally oriented warm anomalies originate from the land and propagate offshore reaching about 350 km by 2100 LST. Subsequently, at 0300 LST, similar cold anomalies emerge from the land and move offshore by 0900 LST. These cold anomalies indicate that the gravity waves induce upward motion of air parcels along their paths, creating a favorable environment for convection and potentially triggering new convective development.

The gravity wave signal is notably stronger in the fast-moving group. For instance, at 2100 LST (Figs. 12b,g), the maximum warm anomalies at around 350 km offshore reach approximately 0.5 K in the fast-moving group, compared with only 0.2 K in the slow-moving group. This difference in magnitude is likely associated with the stronger land–sea thermal contrast in the fast-moving group, which enhances the generation and propagation of gravity waves (Fig. 11). Similarly, the cold anomaly signals are also more pronounced in the fast-moving group, likely suggesting stronger upward motion and more efficient convective triggering.

The rainfall peaks (green lines in Fig. 12) clearly exhibit offshore propagation in both groups. In the fast-moving group, the locations of maxima closely align with the centers of cold anomalies over the ocean (Figs. 12c–e), indicating that gravity waves dominate both the movement and the speed of rainfall propagation. In contrast, at 1500 LST, the rainfall peak in the slow-moving group (Fig. 12j) does not coincide with the cold anomaly center, suggesting that the gravity wave phase propagates faster than the rainfall itself. This observation is consistent with our earlier discussion (section 4a), which indicated that cold pools control the propagation and speed of rainfall under strong low-level wind shear conditions in the slow-moving group.

To verify that the wave seen in Fig. 12 is an inertia–gravity wave, we calculated the vertical wavelength λ_z following the method applied in Chen and Du (2024), which estimates λ_z based on the spacing between positive and negative anomaly peaks in the vertical potential temperature profile. According to the inertia–gravity wave dispersion relation, the horizontal phase speed of gravity waves (Du and Rotunno 2015) can be expressed as

$$c = \frac{N\lambda_z}{2\pi\sqrt{1 - \left(\frac{f}{\omega}\right)^2}} + \overline{u}, \tag{7}$$

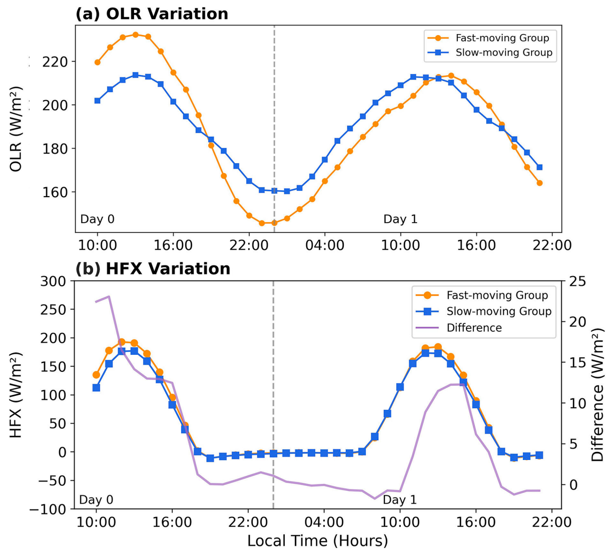

FIG. 10. Time series of land area-averaged (a) OLR and (b) surface heat flux (W m^{-2}).

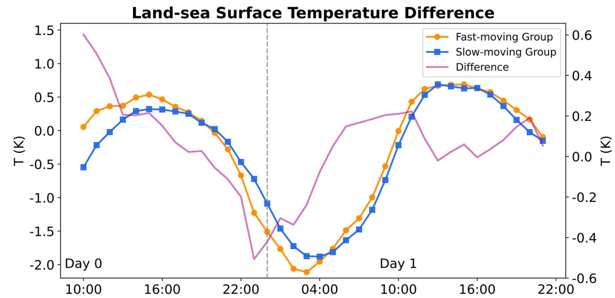

FIG. 11. Temporal evolution of the surface temperature difference between ocean and land (K). The land temperature is averaged over the region within 200 km inland from the coastline, while the ocean temperature is averaged over the marine area within 200 km offshore.

where c represents the horizontal phase speed of the gravity wave and N represents the buoyancy frequency. The $\overline{u}$ is the background wind, f is the Coriolis parameter, and $\omega = 2\pi/T$, where T is the diurnal period (24 h). Based on this formulation, the estimated phase speeds are 11.91 m s^{-1} for the fast-moving group and 11.68 m s^{-1} for the slow-moving group.

To further validate the findings above, the Hovmöller diagrams of potential temperature anomaly averaged from 1 to 3 km are depicted in Figs. 13b and 13c. The white lines show the propagation speed of the gravity wave signal in Fig. 12, which is 11.92 and 11.76 m s^{-1} in the fast- and slow-moving groups, respectively, in close agreement with the phase speed calculated from the inertia–gravity wave dispersion relation above. These results suggest that the signal in Fig. 12 is from inertia–gravity waves, indicating that gravity wave phase speeds alone cannot fully explain the difference in rainfall propagation speed between the two groups and that cold pool dynamics may play a more dominant role in driving the slower propagation in the slow-moving group.

Hovmöller diagrams of CAPE and low-pass-filtered potential temperature perturbations averaged between 3- and 5-km altitude are shown in Fig. 14. In the fast-moving group (Fig. 14a), CAPE remains high (310–340 J kg^{-1}) from 2200 LST on day 0 to 1000 LST on day 1 across a wide offshore extent of 0–600 km, indicating that gravity wave–induced upward motion effectively supports convective development and sustains rainfall propagation. In contrast, in the slow-moving group (Fig. 14b), large CAPE values are confined within 0–300 km from the coast, suggesting weaker gravity wave forcing and indicating that the environment over the ocean is less conducive to convection initiation. Under these conditions, cold pools may serve as the primary mechanism for triggering new convection and sustaining rainfall propagation.

These results suggest that gravity waves dominate rainfall propagation in the fast-moving group, providing evidence consistent with the observations discussed in Fig. 12. In contrast, in the slow-moving group, gravity waves play a secondary role, acting mainly as a preconditioning mechanism that improves the thermodynamic environment over the ocean but does not directly control the speed or extent of rainfall propagation.

c. *Influence of background wind on cold pool propagation*

To further confirm the relationship between rainfall propagation speed and cold pools in the slow-moving group, we examine the correlation between propagation speed and low-level (1-km altitude) wind speed averaged over the region 300–500 km from the coastline, as shown in Fig. 15. The low-level background wind is a key factor influencing the movement speed of cold pools and, consequently, the propagation of convective systems.

In the slow-moving group (Fig. 15b), a positive correlation is observed between rainfall propagation speed and low-level wind speed ($r = 0.685$, $p = 0.042$), suggesting that the background low-level flow may modulate cold pool movement and thereby influence rainfall propagation. Although the sample size is limited and the relationship should be interpreted with caution, it provides suggestive statistical evidence that cold pools play a role in controlling the propagation speed of rainfall in this group. These results are consistent with Dao et al. (2026), who emphasized that low-level winds strongly influence the motion of surface convergence zones associated with cold pools.

In contrast, no significant correlation is found in the fast-moving group (Fig. 15a), suggesting that low-level winds exert minimal influence on rainfall propagation speed. This further supports the conclusion that cold pools are not the primary mechanism governing rainfall propagation in the fast-moving group, where gravity waves play the dominant role instead.

5. Summary and discussion

Rainfall along the northern coast of New Guinea exhibits a clear diurnal cycle, propagating from the coast during the evening to offshore in the morning. Hovmöller diagrams derived from both satellite observations and model simulations reveal a wide range of propagation speeds, even under weak background wind conditions. The mechanisms driving these variabilities in

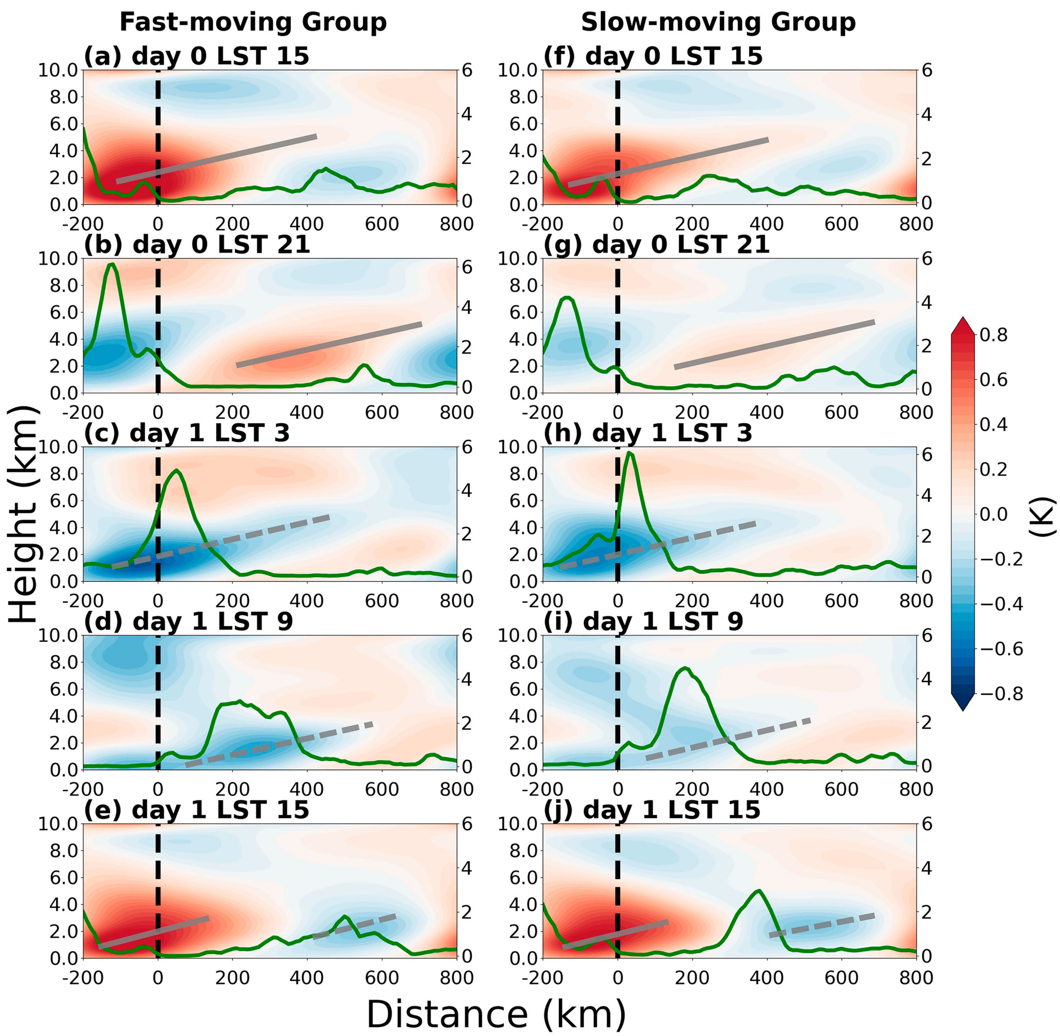

FIG. 12. Diurnal composite zonal cross sections of low-pass-filtered potential temperature anomaly (shading; K) averaged over the orange box shown in Fig. 1 for (a)–(e) the fast-moving group and (f)–(j) slow-moving group. The anomalies are calculated by removing both the time mean and the zonal mean. The gray line represents gravity waves, the solid green line indicates rainfall (mm h^{-1}), and the black dashed line indicates the coastline.

propagation speed have not been well documented, and their exact nature remains unclear. In this study, we investigate a well-validated convection-permitting model simulation for the summers of 2005–15, which successfully captures observed offshore rainfall propagation, to examine these processes in detail. The analysis focuses on objectively identified rainfall propagation events within the model dataset.

The primary conclusions of this study are as follows:

1) Rainfall along the northern coast of New Guinea can propagate more than 600 km offshore, with propagation speeds ranging from 5 to 15 m s^{-1} under weak offshore background wind conditions.
2) Gravity waves are not the sole mechanism responsible for long-distance rainfall propagation. Under strong low-level wind shear, cold pools can also sustain offshore rainfall propagation exceeding 600 km, with an average speed of approximately 8 m s^{-1}, slightly slower than the gravity wave–induced rainfall propagation speed, as illustrated schematically in Fig. 16a.

The variability in rainfall propagation speed arises from the relative dominance of these two mechanisms. Near the coast, rainfall propagation is primarily governed by density currents formed through the combined effects of land breezes and cold pools. In this region, both cold pool intensity and the strength of low-level background winds control the propagation speed. Farther offshore (beyond ~150 km), rainfall propagation associated with gravity waves is faster (~11.5 m s^{-1}). These cases occur under conditions of reduced daytime cloud cover over land, which allows stronger solar heating, enhancing the land–sea thermal contrast, and thereby generating stronger gravity waves. These processes are illustrated schematically in Fig. 16b.

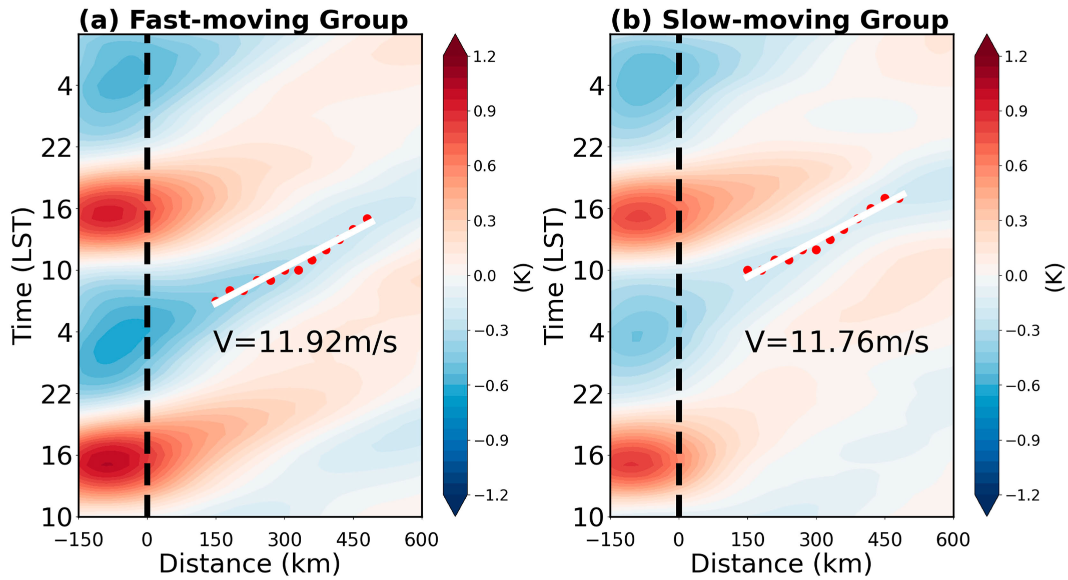

FIG. 13. Hovmöller diagrams of potential temperature anomaly averaged from 1- to 3-km altitude from the (a) fast- and (b) slow-moving groups. The red dots indicate the maximum negative potential temperature anomaly, and the white line is the regression line fitted to the red dots, representing the propagation speed of the gravity wave signal in Fig. 12. The black dashed line represents the location of the coastline.

In contrast, slower-propagation cases ($\sim$8 m s^{-1}) occur under stronger low-level wind shear and greater daytime cloud cover over land. In these environments, gravity waves are weaker, and cold pools generated by coastal convection and nocturnal radiative cooling over land are stronger and spreading over the ocean. Interactions between cold pools and low-level wind shear induce ascent along the leading edge of the cold pool, triggering new convection. As a result, rainfall propagates in a narrow, more organized line that advances offshore more slowly but can still extend beyond 600 km offshore.

While this study identifies gravity waves and cold pool dynamics as two distinct mechanisms governing offshore rainfall propagation in northern New Guinea, the real-world processes are likely more complex. Cold pools generated by deep convection can trigger gravity waves through latent heat release and evaporative cooling, while gravity waves can, in turn, modulate the thermodynamic environment that influence cold pool propagation. The nonlinear interactions between these processes remain insufficiently understood. Future idealized modeling experiments will be valuable for

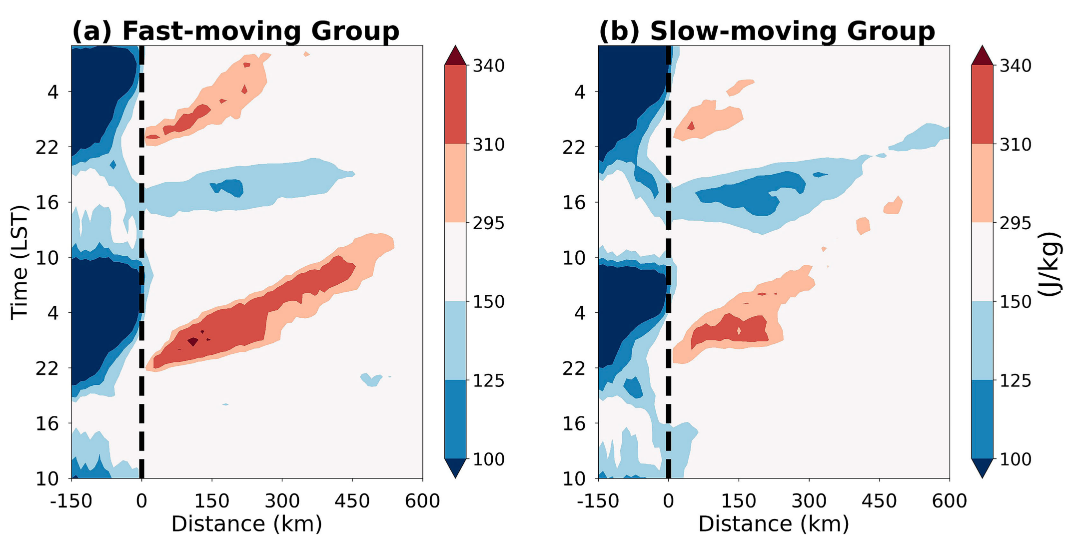

FIG. 14. Hovmöller diagram of CAPE (shading; J kg^{-1}) calculated over the 3–5-km altitude range. The black dashed line indicates the coastline.

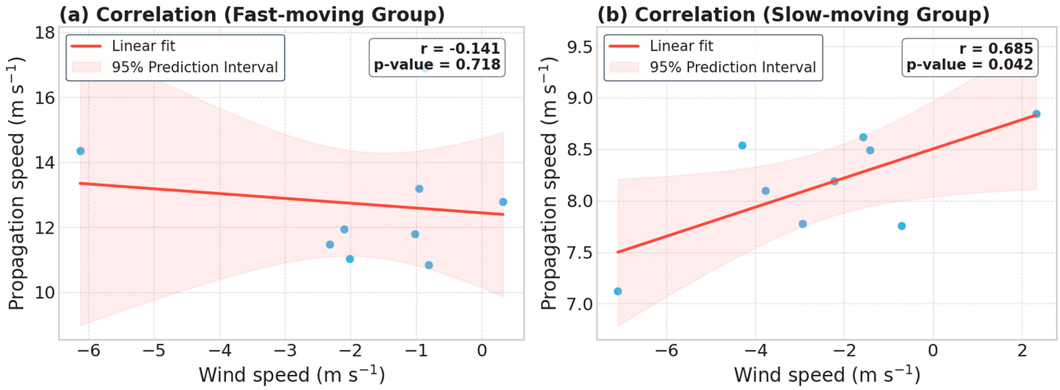

FIG. 15. Scatterplot of low-level wind (1-km altitude) averaged over the region 300–500 km from the coastline vs offshore rainfall propagation speed. The pink shaded area represents the 95% confidence interval, and the red line represents the regression line.

disentangling their interplay and quantifying their relative contributions.

This study focuses on cases with weak offshore background winds (0–2 m s^{-1}) to isolate the effects of gravity waves and cold pools. However, large-scale circulation systems over the Maritime Continent, which were not explicitly considered in this study, can significantly modulate background winds and other environmental factors. For example, the MJO modulates convection, moisture, and wind patterns on intraseasonal time scales (e.g., Ichikawa and Yasunari 2007; Birch et al. 2016), while interannual variability associated with El Niño–Southern Oscillation (ENSO) alters sea surface temperatures, atmospheric stability, and precipitation distributions across the region (e.g., Smith et al. 2013). The Australian monsoon system also plays a crucial role during the austral summer, affecting both background flow and moisture supply (e.g., Gallego et al. 2017). Future work could explore how these large-scale circulations interact with local processes to modulate rainfall propagation. Future research should also aim to validate these findings in this study through dedicated field campaigns incorporating radar networks, radiosondes, and surface measurements. Extending this analysis to other regions and seasons would help assess the generalizability of our results. In addition, idealized modeling frameworks could be employed to better understand the coupled dynamics of gravity waves and cold pools and to quantify their respective roles in organizing tropical convection and diurnal rainfall propagation.

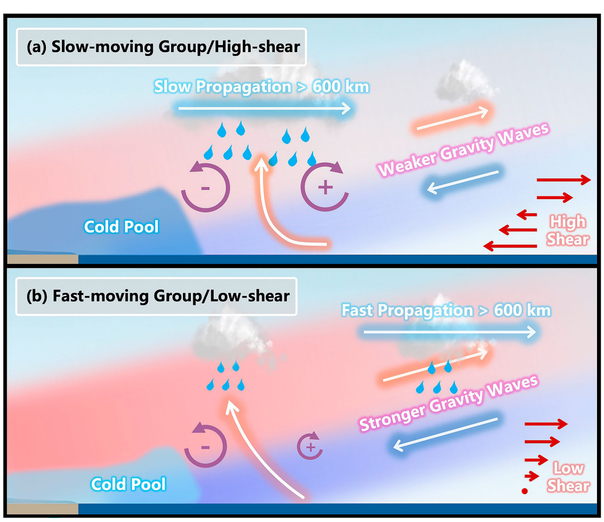

FIG. 16. Schematic diagram of key mechanisms influencing rainfall propagation over New Guinea. (a) Under high wind shear conditions, the cold pool drives slow rainfall propagation offshore, extending beyond 600 km from the coastline. (b) Under low wind shear conditions, the cold pool governs rainfall propagation near the coast, while gravity waves dominate fast propagation farther offshore. Shading represents vertical motion induced by gravity waves.

Acknowledgments. We are very grateful to Cathryn Birch (the University of Leeds), Yi Huang (the University of Melbourne), and Thi Lan Dao (the University of Melbourne) for their helpful comments on this study. Thanks also to two anonymous reviewers for their thoughtful comments and suggestions, which have greatly improved the quality of our manuscript. This study was supported by the Guangdong Major Project of Basic and Applied Basic Research (Grants 2020B0301030004, 2024A1515510005, and 2025A1515011974), the National Natural Science Foundation of China (Grants 42475002 and 42075006), a project supported by the Southern Marine Science and Engineering Guangdong Laboratory (Zhuhai) (SML2024SP035, SML2024SP012, and 311024001), the Key Innovation Team of the China Meteorological Administration (CMA2023ZD08), and the Australian Research Council (ARC) Centre of Excellence for the Weather of the 21st Century (CE230100012). We also acknowledge the high-performance computing support from the National Computing Infrastructure (NCI) National Facility of Australia and the School of Atmospheric Sciences of Sun Yat-sen University.

Data availability statement. The data in this study are available from the corresponding author upon request.

REFERENCES

Bai, H., and Coauthors, 2021: Formation of nocturnal offshore rainfall near the west coast of Sumatra: Land breeze or gravity wave?

Mon. Wea. Rev., **149**, 715–731, https://doi.org/10.1175/MWR-D-20-0179.1.

Birch, C. E., S. Webster, S. C. Peatman, D. J. Parker, A. J. Matthews, Y. Li, and M. E. E. Hassim, 2016: Scale interactions between the MJO and the western Maritime Continent. *J. Climate*, **29**, 2471–2492, https://doi.org/10.1175/JCLI-D-15-0557.1.

Bryan, G. H., and R. Rotunno, 2014: The optimal state for gravity currents in shear. *J. Atmos. Sci.*, **71**, 448–468, https://doi.org/10.1175/JAS-D-13-0156.1.

——, J. C. Knievel, and M. D. Parker, 2006: A multimodel assessment of RKW theory's relevance to squall-line characteristics. *Mon. Wea. Rev.*, **134**, 2772–2792, https://doi.org/10.1175/MWR3226.1.

Chen, X., F. Zhang, and K. Zhao, 2016: Diurnal variations of the land–sea breeze and its related precipitation over south China. *J. Atmos. Sci.*, **73**, 4793–4815, https://doi.org/10.1175/JAS-D-16-0106.1.

Chen, Z., and Y. Du, 2024: The influence of topography on the diurnal rainfall propagation in the Bay of Bengal. *J. Atmos. Sci.*, **81**, 1019–1032, https://doi.org/10.1175/JAS-D-23-0225.1.

——, ——, C. Vincent, E. Short, and H. Yang, 2025: Influence of coastal topography on offshore diurnal rainfall propagation dynamics: A linear gravity wave model approach. *J. Atmos. Sci.*, **82**, 1911–1927, https://doi.org/10.1175/JAS-D-24-0214.1.

Chou, M.-D., and M. J. Suarez, 1994: An efficient thermal infrared radiation parameterization for use in general circulation models. NASA Tech. Memo 3, 102 pp.

Coppin, D., and G. Bellon, 2019: Physical mechanisms controlling the offshore propagation of convection in the tropics: 1. Flat island. *J. Adv. Model. Earth Syst.*, **11**, 3042–3056, https://doi.org/10.1029/2019MS001793.

Dai, A., 2001: Global precipitation and thunderstorm frequencies. Part II: Diurnal variations. *J. Climate*, **14**, 1112–1128, https://doi.org/10.1175/1520-0442(2001)014<1112:GPATFP>2.0.CO;2.

Dao, T., C. Vincent, Y. Huang, S. Peatman, J. Soderholm, C. Birch, and D. Roberts, 2026: Joint modulation of coastal rainfall in northeast Australia by local and large-scale forcings. *Quart. J. Roy. Meteor. Soc.*, **152**, e70027, https://doi.org/10.1002/qj.70027.

Dee, D. P., and Coauthors, 2011: The ERA-Interim reanalysis: Configuration and performance of the data assimilation system. *Quart. J. Roy. Meteor. Soc.*, **137**, 553–597, https://doi.org/10.1002/qj.828.

Du, Y., 2023: Offshore migration of summer monsoon low-level jet on a diurnal scale. *Geophys. Res. Lett.*, **50**, e2023GL103840, https://doi.org/10.1029/2023GL103840.

——, and R. Rotunno, 2015: Thermally driven diurnally periodic wind signals off the east coast of China. *J. Atmos. Sci.*, **72**, 2806–2821, https://doi.org/10.1175/JAS-D-14-0339.1.

——, and ——, 2018: Diurnal cycle of rainfall and winds near the south coast of China. *J. Atmos. Sci.*, **75**, 2065–2082, https://doi.org/10.1175/JAS-D-17-0397.1.

——, ——, and F. Zhang, 2019: Impact of vertical wind shear on gravity wave propagation in the land–sea-breeze circulation at the equator. *J. Atmos. Sci.*, **76**, 3247–3265, https://doi.org/10.1175/JAS-D-19-0069.1.

——, G. Chen, B. Han, L. Bai, and M. Li, 2020: Convection initiation and growth at the coast of South China. Part II: Effects of the terrain, coastline, and cold pools. *Mon. Wea. Rev.*, **148**, 3871–3892, https://doi.org/10.1175/MWR-D-20-0090.1.

——, R. Rotunno, Z. Chen, and H. Yang, 2024: A linear theory for periodic convectively forced gravity waves near a coastline. *J. Atmos. Sci.*, **81**, 1271–1288, https://doi.org/10.1175/JAS-D-23-0173.1.

Fang, J., and Y. Du, 2022: A global survey of diurnal offshore propagation of rainfall. *Nat. Commun.*, **13**, 7437, https://doi.org/10.1038/s41467-022-34842-0.

Fujita, M., K. Yoneyama, S. Mori, T. Nasuno, and M. Satoh, 2011: Diurnal convection peaks over the eastern Indian Ocean off Sumatra during different MJO phases. *J. Meteor. Soc. Japan*, **89A**, 317–330, https://doi.org/10.2151/jmsj.2011-A22.

Gallego, D., R. García-Herrera, C. Peña-Ortiz, and P. Ribera, 2017: The steady enhancement of the Australian summer monsoon in the last 200 years. *Sci. Rep.*, **7**, 16166, https://doi.org/10.1038/s41598-017-16414-1.

Grant, L. D., and S. C. van den Heever, 2016: Cold pool dissipation. *J. Geophys. Res. Atmos.*, **121**, 1138–1155, https://doi.org/10.1002/2015JD023813.

Hassim, M., T. Lane, and W. Grabowski, 2016: The diurnal cycle of rainfall over New Guinea in convection-permitting WRF simulations. *Atmos. Chem. Phys.*, **16**, 161–175, https://doi.org/10.5194/acp-16-161-2016.

Hong, S.-Y., and J.-O. J. Lim, 2006: The WRF single-moment 6-class microphysics scheme (WSM6). *Asia. Pac. J. Atmos. Sci.*, **42**, 129–151.

Houze, R. A., Jr., S. G. Geotis, F. D. Marks Jr., and A. K. West, 1981: Winter monsoon convection in the vicinity of North Borneo. Part I: Structure and time variation of the clouds and precipitation. *Mon. Wea. Rev.*, **109**, 1595–1614, https://doi.org/10.1175/1520-0493(1981)109<1595:WMCITV>2.0.CO;2.

Huffman, G. J., D. T. Bolvin, and E. J. Nelkin, 2015: Integrated Multi-satellitE retrievals for GPM (IMERG) technical documentation. NASA/GSFC Code 612 Tech. Doc., 54 pp., https://pmm.nasa.gov/sites/default/files/document_files/IMERG_doc.pdf.

Ichikawa, H., and T. Yasunari, 2007: Propagating diurnal disturbances embedded in the Madden-Julian Oscillation. *Geophys. Res. Lett.*, **34**, L18811, https://doi.org/10.1029/2007GL030480.

——, and ——, 2008: Intraseasonal variability in diurnal rainfall over New Guinea and the surrounding oceans during austral summer. *J. Climate*, **21**, 2852–2868, https://doi.org/10.1175/2007JCLI1784.1.

Janjić, Z. I., 1994: The step-mountain eta coordinate model: Further developments of the convection, viscous sublayer, and turbulence closure schemes. *Mon. Wea. Rev.*, **122**, 927–945, https://doi.org/10.1175/1520-0493(1994)122<0927:TSMECM2.0.CO;2.

Jiang, Q., 2012: On offshore propagating diurnal waves. *J. Atmos. Sci.*, **69**, 1562–1581, https://doi.org/10.1175/JAS-D-11-0220.1.

Johnson, R. H., 2011: Diurnal cycle of monsoon convection. *The Global Monsoon System: Research and Forecast.* World Scientific, 257–276, https://doi.org/10.1142/9789814343411_0015.

——, and D. L. Priegnitz, 1981: Winter monsoon convection in the vicinity of North Borneo. Part II: Effects on large-scale fields. *Mon. Wea. Rev.*, **109**, 1615–1628, https://doi.org/10.1175/1520-0493(1981)109<1615:WMCITV>2.0.CO;2.

——, and J. F. Bresch, 1991: Diagnosed characteristics of precipitation systems over Taiwan during the May–June 1987 TAMEX. *Mon. Wea. Rev.*, **119**, 2540–2557, https://doi.org/10.1175/1520-0493(1991)119<2540:DCOPSO>2.0.CO;2.

Kikuchi, K., and B. Wang, 2008: Diurnal precipitation regimes in the global tropics. *J. Climate*, **21**, 2680–2696, https://doi.org/10.1175/2007JCLI2051.1.

Kruse, C. G., and R. B. Smith, 2015: Gravity wave diagnostics and characteristics in mesoscale fields. *J. Atmos. Sci.*, **72**, 4372–4392, https://doi.org/10.1175/JAS-D-15-0079.1.

Lane, T. P., 2021: Does lower-stratospheric shear influence the mesoscale organization of convection? *Geophys. Res. Lett.*, **48**, e2020GL091025, https://doi.org/10.1029/2020GL091025.

Li, Y., and R. E. Carbone, 2015: Offshore propagation of coastal precipitation. *J. Atmos. Sci.*, **72**, 4553–4568, https://doi.org/10.1175/JAS-D-15-0104.1.

Love, B. S., A. J. Matthews, and G. M. Lister, 2011: The diurnal cycle of precipitation over the Maritime Continent in a high-resolution atmospheric model. *Quart. J. Roy. Meteor. Soc.*, **137**, 934–947, https://doi.org/10.1002/qj.809.

Mapes, B. E., and R. A. Houze Jr., 1993: Cloud clusters and superclusters over the oceanic warm pool. *Mon. Wea. Rev.*, **121**, 1398–1416, https://doi.org/10.1175/1520-0493(1993)121<1398:CCASOT>2.0.CO;2.

——, T. T. Warner, and M. Xu, 2003: Diurnal patterns of rainfall in northwestern South America. Part III: Diurnal gravity waves and nocturnal convection offshore. *Mon. Wea. Rev.*, **131**, 830–844, https://doi.org/10.1175/1520-0493(2003)131<0830:DPORIN>2.0.CO;2.

Mellor, G. L., and T. Yamada, 1982: Development of a turbulence closure model for geophysical fluid problems. *Rev. Geophys.*, **20**, 851–875, https://doi.org/10.1029/RG020i004p00851.

Mlawer, E. J., S. J. Taubman, P. D. Brown, M. J. Iacono, and S. A. Clough, 1997: Radiative transfer for inhomogeneous atmospheres: RRTM, a validated correlated-*k* model for the longwave. *J. Geophys. Res.*, **102**, 16 663–16 682, https://doi.org/10.1029/97JD00237.

Neale, R., and J. Slingo, 2003: The Maritime Continent and its role in the global climate: A GCM study. *J. Climate*, **16**, 834–848, https://doi.org/10.1175/1520-0442(2003)016<0834:TMCAIR>2.0.CO;2.

Nesbitt, S. W., and E. J. Zipser, 2003: The diurnal cycle of rainfall and convective intensity according to three years of TRMM measurements. *J. Climate*, **16**, 1456–1475, https://doi.org/10.1175/1520-0442-16.10.1456.

Ohsawa, T., H. Ueda, T. Hayashi, A. Watanabe, and J. Matsumoto, 2001: Diurnal variations of convective activity and rainfall in tropical Asia. *J. Meteor. Soc. Japan*, **79**, 333–352, https://doi.org/10.2151/jmsj.79.333.

Peatman, S. C., and Coauthors, 2023: The role of density currents and gravity waves in the offshore propagation of convection over Sumatra. *Mon. Wea. Rev.*, **151**, 1757–1777, https://doi.org/10.1175/MWR-D-22-0322.1.

Peng, C. H., and X. Chen, 2023: Warm-season afternoon precipitation peak in the central Bay of Bengal: Process-oriented diagnostics. *J. Geophys. Res. Atmos.*, **128**, e2022JD038398, https://doi.org/10.1029/2022JD038398.

Peng, C.-H., and X. Chen, 2024: Monsoonal MCS initiation, rainfall, and diurnal gravity waves over the Bay of Bengal: Observation and a linear model. *J. Atmos. Sci.*, **81**, 1401–1418, https://doi.org/10.1175/JAS-D-23-0230.1.

——, and ——, 2025: Mesoscale processes driving offshore MCS initiation in the South Asian summer monsoon: Insights from an ensemble-based satellite data assimilation experiment. *J. Atmos. Sci.*, **82**, 1381–1402, https://doi.org/10.1175/JAS-D-24-0231.1.

Qian, T., C. C. Epifanio, and F. Zhang, 2009: Linear theory calculations for the sea breeze in a background wind: The equatorial case. *J. Atmos. Sci.*, **66**, 1749–1763, https://doi.org/10.1175/2008JAS2851.1.

——, ——, and ——, 2012: Topographic effects on the tropical land and sea breeze. *J. Atmos. Sci.*, **69**, 130–149, https://doi.org/10.1175/JAS-D-11-011.1.

Rotunno, R., 1983: On the linear theory of the land and sea breeze. *J. Atmos. Sci.*, **40**, 1999–2009, https://doi.org/10.1175/1520-0469(1983)040<1999:OTLTOT>2.0.CO;2.

——, J. B. Klemp, and M. L. Weisman, 1988: A theory for strong, long-lived squall lines. *J. Atmos. Sci.*, **45**, 463–485, https://doi.org/10.1175/1520-0469(1988)045<0463:ATFSLL>2.0.CO;2.

Ruppert, J. H., Jr., and F. Zhang, 2019: Diurnal forcing and phase locking of gravity waves in the Maritime Continent. *J. Atmos. Sci.*, **76**, 2815–2835, https://doi.org/10.1175/JAS-D-19-0061.1.

——, R. H. Johnson, and A. K. Rowe, 2013: Diurnal circulations and rainfall in Taiwan during SoWMEX/TiMREX (2008). *Mon. Wea. Rev.*, **141**, 3851–3872, https://doi.org/10.1175/MWR-D-12-00301.1.

——, X. Chen, and F. Zhang, 2020: Convectively forced diurnal gravity waves in the Maritime Continent. *J. Atmos. Sci.*, **77**, 1119–1136, https://doi.org/10.1175/JAS-D-19-0236.1.

Sakurai, N., and Coauthors, 2009: Internal structures of migratory cloud systems with diurnal cycle over Sumatera Island during CPEA-I campaign. *J. Meteor. Soc. Japan*, **87**, 157–170, https://doi.org/10.2151/jmsj.87.157.

Short, E., C. L. Vincent, and T. P. Lane, 2019: Diurnal cycle of surface winds in the Maritime Continent observed through satellite scatterometry. *Mon. Wea. Rev.*, **147**, 2023–2044, https://doi.org/10.1175/MWR-D-18-0433.1.

Skamarock, W. C., and J. B. Klemp, 2008: A time-split nonhydrostatic atmospheric model for weather research and forecasting applications. *J. Comput. Phys.*, **227**, 3465–3485, https://doi.org/10.1016/j.jcp.2007.01.037.

Smith, I., A. Moise, K. Inape, B. Murphy, R. Colman, S. Power, and C. Chung, 2013: ENSO-related rainfall changes over the New Guinea region. *J. Geophys. Res. Atmos*, **118**, 10 665–10 675, https://doi.org/10.1002/jgrd.50818.

Tripoli, G. J., and W. R. Cotton, 1989: Numerical study of an observed orogenic mesoscale convective system. Part 2: Analysis of governing dynamics. *Mon. Wea. Rev.*, **117**, 305–328, https://doi.org/10.1175/1520-0493(1989)117<0305:NSOAOO>2.0.CO;2.

Vincent, C. L., and T. P. Lane, 2016a: Evolution of the diurnal precipitation cycle with the passage of a Madden–Julian oscillation event through the Maritime Continent. *Mon. Wea. Rev.*, **144**, 1983–2005, https://doi.org/10.1175/MWR-D-15-0326.1.

——, and ——, 2016b: Maritime Continent Austral summer climatology v1.0. NCI National Research Data Collection, accessed 1 May 2018, https://doi.org/10.4225/41/5850b633c54ed.

——, and ——, 2017: A 10-year austral summer climatology of observed and modeled intraseasonal, mesoscale, and diurnal variations over the Maritime Continent. *J. Climate*, **30**, 3807–3828, https://doi.org/10.1175/JCLI-D-16-0688.1.

——, and ——, 2018: Mesoscale variation in diabatic heating around Sumatra, and its modulation with the Madden–Julian oscillation. *Mon. Wea. Rev.*, **146**, 2599–2614, https://doi.org/10.1175/MWR-D-17-0392.1.

Weisman, M. L., and R. Rotunno, 2004: "A theory for strong long-lived squall lines" revisited. *J. Atmos. Sci.*, **61**, 361–382, https://doi.org/10.1175/1520-0469(2004)061<0361:ATFSLS>2.0.CO;2.

Yang, G.-Y., and J. Slingo, 2001: The diurnal cycle in the tropics. *Mon. Wea. Rev.*, **129**, 784–801, https://doi.org/10.1175/1520-0493(2001)129<0784:TDCITT>2.0.CO;2.

Yang, H., and Y. Du, 2024: Difference between upshear- and downshear-propagating waves associated with the development of squall lines. *Mon. Wea. Rev.*, **152**, 1399–1420, https://doi.org/10.1175/MWR-D-23-0109.1.

——, and ——, 2026: Distinct convection initiation near and far ahead of an idealized squall line. *J. Atmos. Sci.*, **83**, 151–168, https://doi.org/10.1175/JAS-D-25-0073.1.

Yang, S., and E. A. Smith, 2006: Mechanisms for diurnal variability of global tropical rainfall observed from TRMM. *J. Climate*, **19**, 5190–5226, https://doi.org/10.1175/JCLI3883.1.

Yokoi, S., S. Mori, M. Katsumata, B. Geng, K. Yasunaga, F. Syamsudin, Nurhayati, and K. Yoneyama, 2017: Diurnal cycle of precipitation observed in the western coastal area of Sumatra Island: Offshore preconditioning by gravity waves. *Mon. Wea. Rev.*, **145**, 3745–3761, https://doi.org/10.1175/MWR-D-16-0468.1.

Zhang, J., and Y. Du, 2025: Revisiting the diurnal pulses of tropical cyclones over the northwest Pacific Ocean. *Geophys. Res. Lett.*, **52**, e2025GL116554, https://doi.org/10.1029/2025GL116554.